Available online at www.sciencedirect.com
ScienceDirect
International Journal of Thermal Sciences 47 (2008) 221–228
International Journal of Thermal Sciences
www.elsevier.com/locate/ijts

Deformation and oscillations of a single gas bubble rising in a narrow vertical tube

Zhaoyuan Wang, Albert Y. Tong *

Department of Mechanical and Aerospace Engineering, University of Texas at Arlington, Arlington, TX 76019, USA

Received 9 July 2006; received in revised form 16 February 2007; accepted 17 February 2007

Available online 12 April 2007

Abstract

A single gas bubble rising in a narrow vertical tube is investigated via a numerical model on a 3-D axisymmetric computational domain. The transient governing equations are solved by a finite volume scheme with a two-step projection method. The interface between the liquid and gas phase is tracked by a coupled level set and volume-of-fluid (CLSVOF) method. A surface tension modeling method, which preserves the jump discontinuity of pressure at the interface, is employed. The velocity distribution around the bubble and the bubble rise velocity obtained in the numerical simulation are in excellent agreement with experimental measurements. Special attention is paid to the bubble oscillations during the initial stage of ascent. It has been found that the bubble bottom undergoes severe oscillations while the nose maintains a stable shape. A parametric study is performed to identify the factors controlling the oscillations at the bubble bottom.

Keywords: Single gas bubble; Vertical tube; Oscillations; Interface tracking

1. Introduction

Bubble-driven flows appear in various natural and industrial processes with a wide range of applications such as oil transportation, steam generation, cooling systems of nuclear power plants, propagation of sound in the ocean, cloud cavitations, etc. Numerous experimental and theoretical studies have been carried out during the past fifty years [1–8]. Due to the complex two-phase flow patterns associated with bubble behavior, some issues are still unresolved. In recent years, bubble oscillations have attracted much attention as a result of the development of advanced measurement techniques and tools that provide more detailed information on the dynamics of bubble motion. Bubble oscillations are complicated phenomena that include the bubble rising trajectory and shape instabilities as well as the associated velocity and pressure fluctuations. These oscillations further complicate the bubble flow problems and cast doubt on the accuracy of the terminal velocity and the existence of a "steady state".

Many experimental studies have been reported on the bubble trajectory and shape oscillations [9–12]. Most of the experiments were conducted in an infinite fluid environment where the wall effects of the containers were negligible. Although bubble oscillations in a confined tube or pipe have practical significance, studies on the subject are relatively scarce. If a large bubble is confined in a narrow tube with a comparable cross-sectional diameter, the bubble will rise along the tube centerline, and path instabilities that might occur in unbounded domain will not appear. The problem seems to become somewhat simpler without trajectory oscillations and is therefore often neglected by researchers. Typically, for a large bubble in a narrow tube, a 'slug flow' will develop. This is characterized by a rounded cap front with a long main body surrounded by a falling annular liquid film [2].

Most studies on slug flows have focused on terminal velocity, steady shape and drag force. In a recent study [3], a universal correlation for the rise velocity of a long gas bubble in stagnant fluids contained in a vertical tube was obtained based on data collected from published literature. The velocity field in the liquid around the bubble has been investigated using Particle Image Velocimetry (PIV) by some researchers [4–6]. However, due to experimental difficulties, velocity profiles in

* Corresponding author. Tel.: +1 817 272 2297; fax: +1 817 272 2952.
E-mail address: tong@uta.edu (A.Y. Tong).

1290-0729/$ – see front matter
doi:10.1016/j.ijthermalsci.2007.02.011

Nomenclature

A_s	arbitrary amplitude	
D	tube diameter	mm
Eo	Eötvös number	
F	VOF function	
f	frequency	Hz
g	gravitational acceleration	$\mathrm{m\,s^{-2}}$
h	grid spacing	mm
L	tube length	mm
Mo	Morton number	
J_s	Bessel function	
k	wave number	
n	normal vector	
P	pressure	Pa
r	radial coordinate	mm
R	bubble radius	mm
t	time	ms
u	velocity	$\mathrm{m\,s^{-1}}$
z	axial coordinate	mm

Greek letters

ϕ	level set function	
Φ	velocity potential	
ω	angular frequency	
ε	arbitrary phase angle	
ρ	density	$\mathrm{kg\,m^{-3}}$
σ	surface tension coefficient	$\mathrm{kg\,s^{-2}}$
μ	dynamic viscosity	$\mathrm{kg\,m^{-1}\,s^{-1}}$
κ	local curvature at interface	

Subscripts

g	gas
l	liquid
v	vapor
T	terminal velocity

(All other symbols are defined where they appear.)

the gas phase were seldom available. In the case of numerical simulations, the momentum equations and hence flow calculations were often ignored in the gas phase due to the large density ratio between liquid and gas [7]. Polonsky et al. [8] reported the oscillatory motion of the bubble bottom for a long gas bubble rising in a vertical tube while the nose of the bubble retained its shape. The amplitude of oscillations was found to increase with the bubble length, while the frequency remained constant. van Hout et al. [4] investigated the velocity field induced by a Taylor bubble rising in stagnant liquid. Velocity fluctuations were noticeable fifty tube diameters away from the wake of the bubble. It should be noted that the experimental measurements were performed at steady state while the transient effect was not accounted for in the last two studies.

In the present study, the motion of a single gas bubble, with a diameter comparable to that of the tube, rising through a stagnant liquid is investigated via a numerical method. The transient governing equations are solved by a finite volume scheme with a two-step projection method. The interface between the liquid and gas phase is tracked by a coupled level set and volume-of-fluid (CLSVOF) method. A new surface tension modeling method, termed the pressure boundary method (PBM), is employed. The objective of the present work is to investigate the bubble oscillations during the initial acceleration stage. The velocity field and pressure distribution within the bubble and in the surrounding liquid are also examined.

2. Numerical formulations

2.1. Governing equations

For two-phase flows, the whole flow domain can be described by a single set of momentum and continuity equations within the "one-fluid" formulation approach, where different fluid properties are considered in each individual phase. Proper stress conditions at the interface between different phases can be enforced implicitly. Fluid properties, such as density and viscosity are assumed to be constant in the liquid and gas phase. The governing equations can be written as:

$$\nabla \cdot u = 0 \tag{1}$$

$$\frac{\partial u}{\partial t} + u \cdot \nabla u = -\frac{1}{\rho}\nabla P + \frac{1}{\rho}\nabla \cdot \mu\left[(\nabla u) + (\nabla u)^T\right] + g \tag{2}$$

where u is the velocity, ρ the effective density, P the pressure, μ the effective dynamic viscosity and g the gravitational acceleration. A new surface tension force model is adopted where the surface tension effect is treated as a pressure jump condition at the interface [13]. The model has been shown to be an accurate and efficient method with spurious currents at the interface greatly suppressed. The effective density and viscosity at each grid point are given by:

$$\rho = \rho_g(1 - F) + \rho_l F \tag{3}$$

$$\mu = \mu_g(1 - F) + \mu_l F \tag{4}$$

where F is the VOF function which is zero in the gas phase and one in the liquid. Subscripts g and l denote gas and liquid respectively.

Eq. (2) is approximated in finite-difference form as:

$$\frac{u^{n+1} - u^n}{\delta t} = -u^n \cdot \nabla u^n + g^n - \frac{1}{\rho^n}\nabla P^{n+1} + \frac{1}{\rho^n}\nabla \cdot \mu\left[(\nabla u^n) + (\nabla u^n)^T\right] \tag{5}$$

A two-step projection algorithm is used where Eq. (5) is decomposed into the following two equations:

$$\frac{u^* - u^n}{\delta t} = -u^n \cdot \nabla u^n + g^n - \frac{1}{\rho^n}\nabla P_1 + \frac{1}{\rho^n}\nabla \cdot \mu\left[(\nabla u^n) + (\nabla u^n)^T\right] \tag{6}$$

and

$$\frac{u^* - u^{n+1}}{\delta t} = -\frac{1}{\rho^n}\nabla P_2^{n+1} \tag{7}$$

where u^* represents an intermediate velocity. Pressure P in Eq. (5) is split into two terms, P_1 and P_2. Pressure P_1, accounting for the surface tension effect, is obtained by solving the following pressure equation:

$$\nabla \cdot \left[\frac{1}{\rho^n}\nabla P_1\right] = 0 \tag{8}$$

with the jump conditions induced by the surface tension effect serving as the boundary condition.

In the first step, an intermediate velocity field, u^*, is computed from Eq. (6), which accounts for incremental changes resulting from viscosity, advection, gravity, and surface tension effect. In the second step, the velocity field, u^{n+1}, is projected into a zero-divergence vector field, resulting in a single Poisson equation for the pressure P_2 given by:

$$\nabla \cdot \left[\frac{1}{\rho^n}\nabla P_2^{n+1}\right] = \frac{\nabla \cdot u^*}{\delta t} \tag{9}$$

Pressure P_2, resulting from flow motion, ensures mass conservation.

2.2. CLSVOF method

The main complexity of the numerical simulation is the dynamics of a rapidly moving interface, the location of which is unknown and is needed as part of the solution. In recent years, a number of methods have been developed for modeling free surface flows [14], among which the volume-of-fluid (VOF) method and the level set (LS) method are two Eulerian-based methods that have been widely used. One of the advantages offered by these methods is the ease in which flow problems with large topological changes and interface deformations can be handled. These include liquid ligament breakup, bubble merging and bursting, and droplet elongation and breakup. The VOF method has the desirable property of mass conservation. However, it lacks accuracy on the normal and curvature calculations due to the discontinuous spatial derivatives of the VOF function near the interface. This may lead to convergence problems especially in the surface tension force dominated problems. As for the LS method, the normal and curvature can be calculated accurately from the continuous and smooth distance functions. However, one serious drawback of this method is the frequent violation of the mass conservation. To overcome such weaknesses of the LS and VOF methods, a coupled level set and volume-of-fluid (CLSVOF) method has recently been reported [15,16].

The LS function, ϕ, is defined as a signed distance function given by:

$$\phi(x,t) = \begin{cases} > 0, & \text{outside the interface} \\ = 0, & \text{at the interface} \\ < 0, & \text{inside the interface} \end{cases} \tag{10}$$

i.e. positive in the liquid, negative in the air, and zero at the interface. The VOF function, F, is defined as the liquid volume fraction in a cell with its value between zero and one in a surface cell and at zero and one in air and liquid respectively, i.e.

$$F(x,t) = \begin{cases} 1, & \text{in the liquid} \\ 0 < F < 1, & \text{at the interface} \\ 0, & \text{external to liquid} \end{cases} \tag{11}$$

The LS function and the VOF function are advanced by the following equations, respectively:

$$\frac{\mathrm{D}\phi}{\mathrm{D}t} = \frac{\partial \phi}{\partial t} + (u \cdot \nabla)\phi = 0 \tag{12}$$

$$\frac{\mathrm{D}F}{\mathrm{D}t} = \frac{\partial F}{\partial t} + (u \cdot \nabla)F = 0 \tag{13}$$

Since the VOF function is not smoothly distributed at the interface, an interface reconstruction procedure is required to evaluate the VOF flux across an interfacial cell. In this study, the interface is reconstructed via a piecewise linear interface construction (PLIC) scheme, and the interface normal is calculated from the LS function as:

$$n = \frac{\nabla \phi}{|\nabla \phi|} \tag{14}$$

It should be noted that the LS function would fail to be a distance function after being advanced by Eq. (12), and a re-initialization process is needed for its return to a distance function. This is achieved by obtaining a steady-state solution of the following re-initialization equation:

$$\frac{\partial \phi}{\partial t} = \frac{\phi_0}{\sqrt{\phi_0^2 + h^2}}\big(1 - |\nabla \phi|\big) \tag{15}$$

where ϕ_0 is the LS function at the previous time step, t the artificial time, and h the grid spacing. Finally, in order to achieve mass conservation, the LS functions have to be re-distanced [15] prior to being used. The curvature, computed directly from the LS function, is given by:

$$\kappa = \nabla \cdot \left(\frac{\nabla \phi}{|\nabla \phi|}\right) \tag{16}$$

Details of CLSVOF scheme employed in the present study can be found in [17].

3. Results and discussion

Initially, a spherical air bubble with a diameter of 20 mm is stationed near the bottom of a vertical tube ($D = 25$ mm and $L = 150$ mm) containing quiescent water. The no-slip boundary condition is imposed at the solid wall with an open boundary condition applied at the top of the tube. The calculations are carried out on an axisymmetric computational domain. Unless otherwise stated, air and water with the following constant properties are used in the simulations: $\rho_l = 1000\ \mathrm{kg\,m^{-3}}$, $\rho_g = 1.226\ \mathrm{kg\,m^{-3}}$, $\mu_l = 1.137 \times 10^{-3}\ \mathrm{kg\,ms^{-1}}$, $\mu_g = 1.78 \times 10^{-5}\ \mathrm{kg\,ms^{-1}}$ with $g = 9.8\ \mathrm{m\,s^{-2}}$, and $\sigma = 0.0728\ \mathrm{kg\,s^{-2}}$. The key dimensionless parameters used in this study include: Morton number $Mo = g v^4 \rho_l^3/\sigma^3$, Eötvös number $Eo = \rho_l g D^2/\sigma$, density ratio ρ_l/ρ_g and viscosity ratio μ_l/μ_g. To validate the accuracy of the numerical method employed in the present study, a grid refinement test is performed first. The results are presented in Appendix A.

3.1. Dynamics of bubble motion and deformation

The time evolution of bubble shapes is shown in Fig. 1(a). The bubble, exerted by buoyancy force, rises rapidly after its release. This ascension process proceeds with the bubble deforming from the initial spherical shape to the final bullet-like shape. The bottom of the bubble moves rapidly upward and develops into a concave shape. It then rebounds downward immediately into a convex shape. This up-and-down oscillatory movement of the bubble bottom continues as the bubble rises with decreasing amplitude. The top of the bubble, on the contrary, remains a spherical cap shape with very little deformation as it ascends.

The velocity field at a time instant is presented in Fig. 1(b) with the corresponding streamline plot shown on the left. The magnified views of several regions around the bubble are presented in Fig. 2. The axial velocity along the center axis of the tube decreases rapidly upward away from the bubble tip and is negligible half a diameter away from the bubble nose (Fig. 2(a)). The radial velocity increases radially away from the tip of the bubble nose followed by the entrance of the fluid into the falling liquid film near the tube wall. Across the

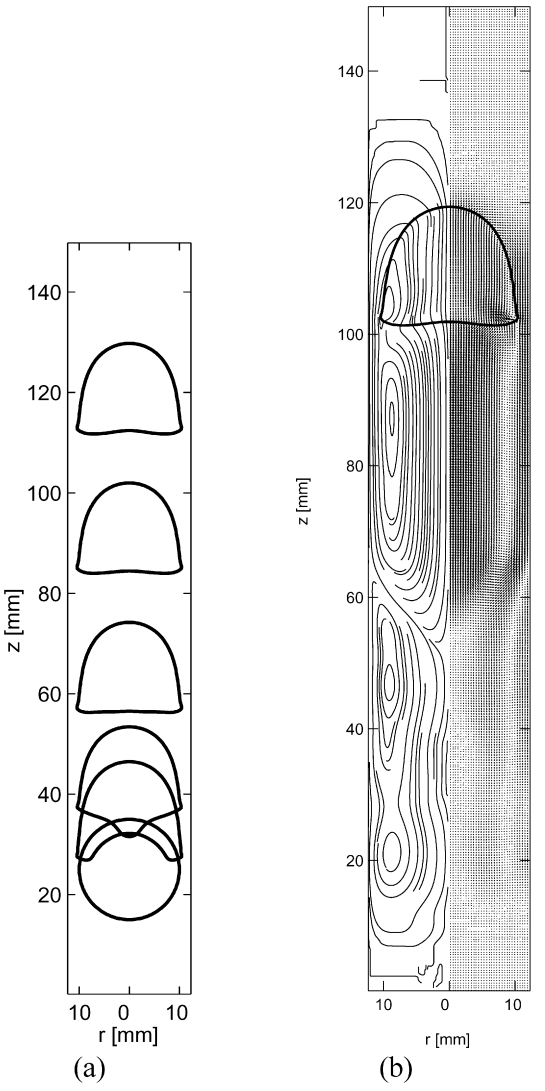

Fig. 1. (a) Time dependent deformation sequence of a single air bubble in a narrow tube. (b) Velocity vector field and streamline plot at one time instant.

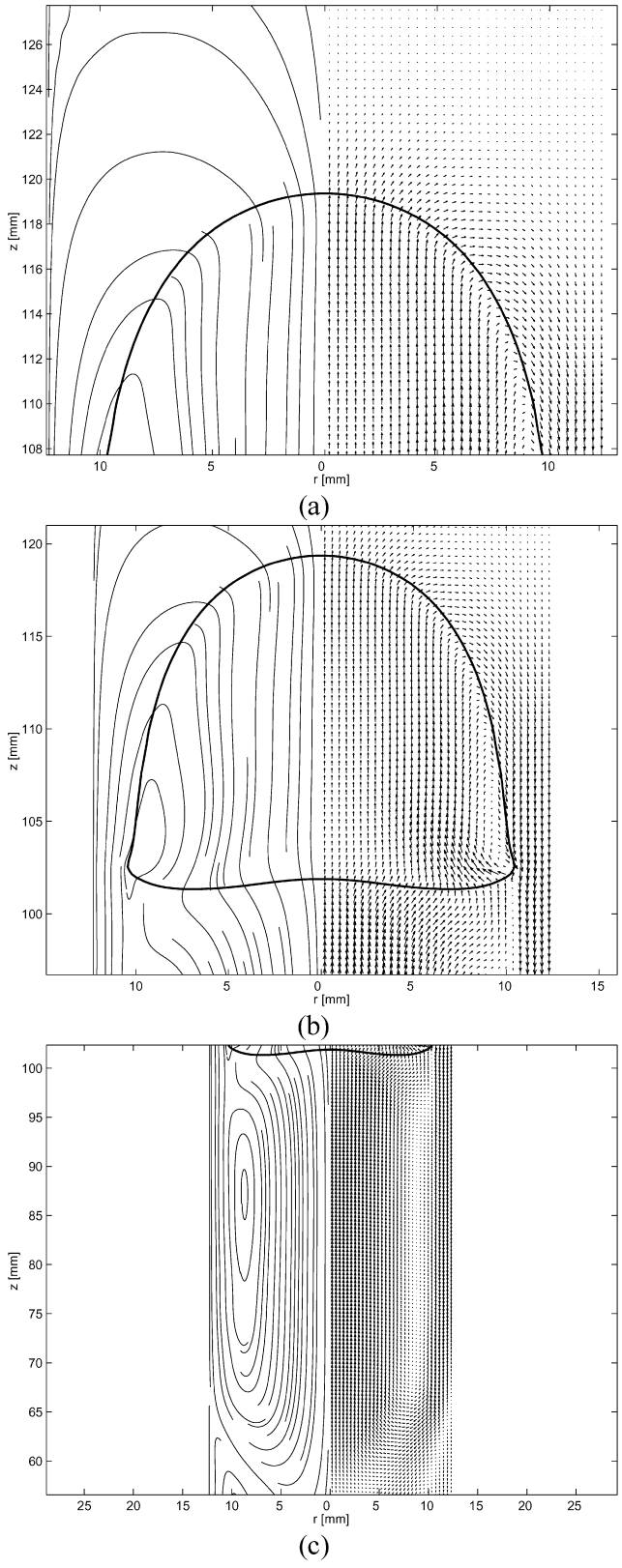

Fig. 2. Velocity field (magnified views): (a) top region; (b) side region; (c) wake region.

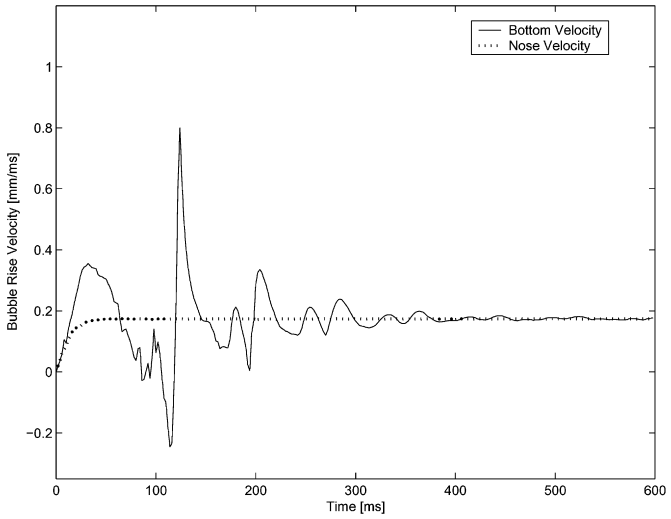

Fig. 3. The axial velocity versus time at the nose and bottom of the bubble.

bubble interface, the flow reverses from upward inside the bubble to downward in the liquid (Fig. 2(b)). In the wake region of the bubble, the downward flow in the liquid film near the tube wall mixes with the liquid slug induced by the gas bubble at approximately two diameters below the bottom of the bubble (Fig. 2(c)). As a result, a toroidal vortex is generated, followed immediately by a much weaker counter-rotating vortex (Fig. 1(b)). It should be mentioned that the observations of the flow structure in the present numerical study are in good agreement with the findings reported in previous experimental studies on slug flows [4–6].

Fig. 3 shows the axial velocity versus time plot at the top and bottom centers of the bubble. The velocity at the bottom undergoes significant oscillations initially and subsides into a steady state gradually. These oscillations at the bottom appear to have no influence on the behavior of the bubble nose, where the velocity rapidly accelerates and immediately reaches a constant value of around 0.1735 mm ms^{-1}. This is in excellent agreement with the terminal velocity of 0.1732 mm ms^{-1} obtained by the correlation $U_T = 0.35\sqrt{gD}$ reported in the literature [2,5].

The pressure contours and the pressure distribution along the axial direction are shown in Figs. 4(a) and (b) respectively. The top of the tube is open to the atmosphere, and thus an open boundary condition is applied there with the atmospheric pressure taken as zero. As shown in Fig. 4(a), the pressure increases gradually with depth from top to bottom, except in the gas phase where it stays constant. Fig. 4(b) shows the axial pressure distribution at three radial positions. The fluid motion is relatively weak in the region from the top of the tube to the nose of the bubble with an almost linear increase in pressure. In the region from the top to bottom of the bubble, the pressure maintains a constant value inside the bubble and changes non-linearly in the liquid film. In the wake region of the bubble, the pressure changes non-linearly in the first recirculation zone beyond which the pressure varies approximately linearly again when the flow diminishes. It is also shown that the pressure variation in the radial direction is very small except near the bubble interface where a pressure jump induced by the surface tension exists.

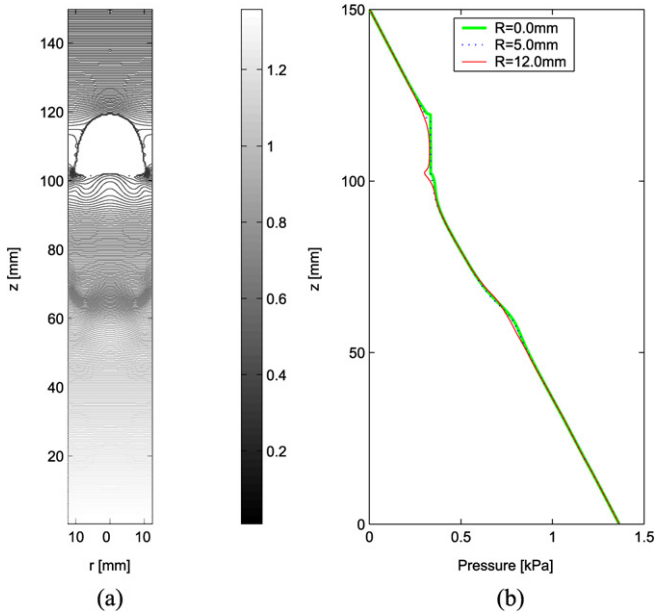

Fig. 4. (a) Pressure contour plot. (b) Pressure distribution along the centerline of the tube at various radial positions.

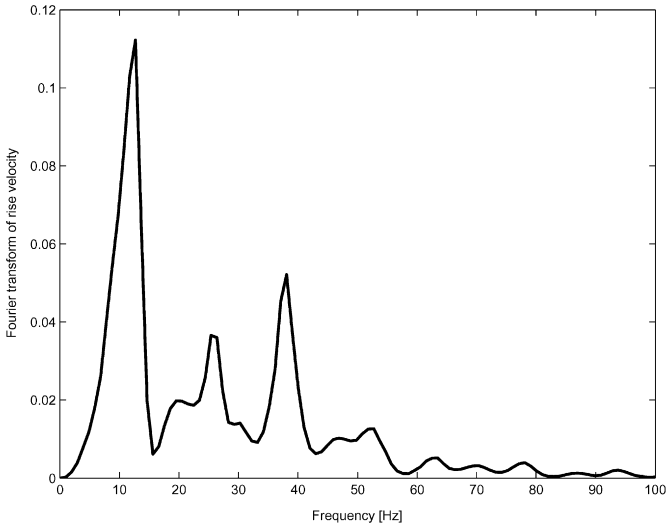

Fig. 5. Power spectra for the oscillations of the bottom velocity.

3.2. Bubble oscillations

As discussed previously, during the acceleration process, significant bubble deformation occurs. This is characterized by oscillatory motion at the bottom with a relatively stable spherical cap shape maintained at the nose (see Fig. 1(a)). This is also manifested by the velocity fluctuations at the bottom as shown in Fig. 3. The velocity at the nose quickly reaches the terminal velocity and remains constant, while the velocity at the bottom undergoes severe oscillations. The Fourier transforms of the bottom velocity are obtained to correlate and analyze the oscillation characteristics. Power spectra of the bubble bottom

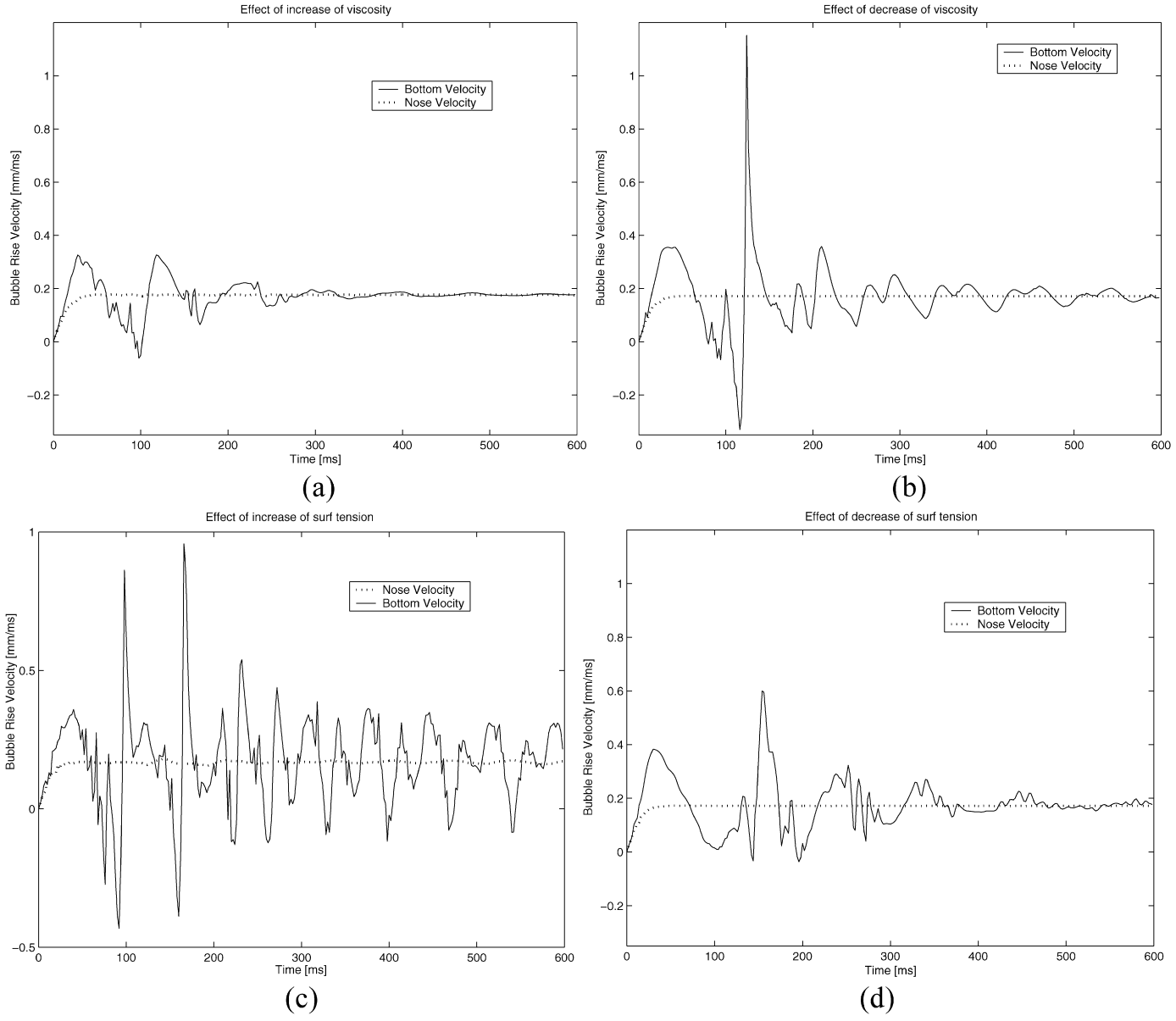

Fig. 6. Bubble rise velocity at the nose and bottom for different cases: (a) high viscosity (10υ); (b) low viscosity (0.1υ); (c) high surface tension (2.0σ); (d) low surface tension (0.5σ).

velocity oscillations are given in Fig. 5. Note that the dominant frequency of the bottom velocity oscillations is approximately 12.7 Hz.

It is of interest to compare the numerical results of the present study with theoretical calculations in order to validate the accuracy of the numerical simulation. In a recent study [8] of the time-dependent characteristics of the motion of an elongated bubble in a vertical pipe, the bubble bottom is treated as a circular liquid membrane modeled by potential flow theory. The velocity potential, Φ, is governed by the Laplace equation:

$$\nabla^2 \Phi = 0 \tag{17}$$

with a solution given by:

$$\Phi(r, \theta, Y, t) = A_s J_s(kr) \cos(s\theta) \mathrm{e}^{kz + \mathrm{i}(\omega t + \varepsilon)} \tag{18}$$

where A_s is the arbitrary amplitude, J_s the Bessel function of the first kind of order s, k the wave number, ω the angular frequency, and ε the arbitrary phase angle. The derivation follows that of Lamb [18] where a more detailed discussion of the solution can be found. The wave number k is determined by the condition that the radial velocity at the rim of the bubble bottom is zero, i.e.,

$$\left.\frac{\partial \Phi}{\partial r}\right|_{r=R} = 0 \tag{19}$$

Due to the symmetrical oscillation character of the bubble bottom imposed in the present numerical simulation, s is taken as zero, and Eq. (19) becomes:

$$J_0'(kr)|_{r=R} = 0 \tag{20}$$

The oscillation frequency, $f(=\frac{\omega}{2\pi})$, can then be obtained by substituting k into the gravity-capillary wave dispersion relation below:

$$\omega = gk + \frac{\sigma}{\rho}k^3 \tag{21}$$

For a bubble bottom radius of 10.6 mm, the oscillation frequency corresponding to the lowest mode is 13.3 Hz. This is in good agreement with the value of 12.7 Hz obtained in the present numerical simulation. In the experimental investigation conducted by Polonsky et al. [8], anti-symmetric oscillations of the bubble bottom were observed for a long gas bubble rising in a tube. These anti-symmetric oscillations were sustained throughout the whole duration of the bubble rising process. It should be noted that, for bubbles with small L/D (length to diameter) values, oscillations at the bubble bottom are very weak with negligible amplitudes and dominant frequencies (see Figs. 3, 8 and 9 of [8]). The bubbles considered in this study are very short in length with an L/D value approximately 0.8 at steady state as shown in Fig. 1. Therefore, the anti-symmetric oscillations can be neglected when the bubble reaches steady state.

3.3. Effects of fluid parameters on the oscillations

A number of cases for different fluid parameters are investigated to identify the factors controlling the oscillatory behaviors of bubble velocity and shape. Figs. 6(a) and (b) show the velocity versus time plot for cases with different liquid viscosities. The liquid viscosity values used are 10.0 times that of water in case (a), and 0.1 times in case (b). It can be seen that an increase in liquid viscosity leads to a decrease in oscillation amplitude and overall duration with larger amplitude and longer overall duration attained by reduction in liquid viscosity. This implies that liquid viscosity has a damping effect on the oscillations, as expected. However, as shown in Fig. 7(a), the oscillation frequency is relatively unaffected by the variation in liquid viscosity. The dominant frequencies for all three cases with different viscosities are almost identical. The gas viscosity plays a negligible role in the bubble motion and is therefore ignored.

Figs. 6(c) and (d) show rise velocity versus time plots for cases with different surface tension coefficients. The surface tension coefficient values considered are twice and half that of water and air. With larger surface tension force, the oscillations become stronger in that both the amplitude and the frequency are increased. With decreased surface tension force, both the amplitude and frequency are decreased. Power spectra of bottom velocity oscillations with different surface tension coefficients are shown in Fig. 7(b). It can be seen that the dominant frequency increases with increase in surface tension.

It should be noted that for all the cases discussed above, $Mo < 2.56 \times 10^{-7}$ and $Eo > 42.0$. According to the *Eo–Re* diagram (Fig. 2.5 of Clift et al. [1]), the bubble will take on a "spherical-cap" shape in an unbounded liquid under these conditions. However, the bubble considered in the current study is confined in a narrow tube. As shown in Fig. 8, the bubble

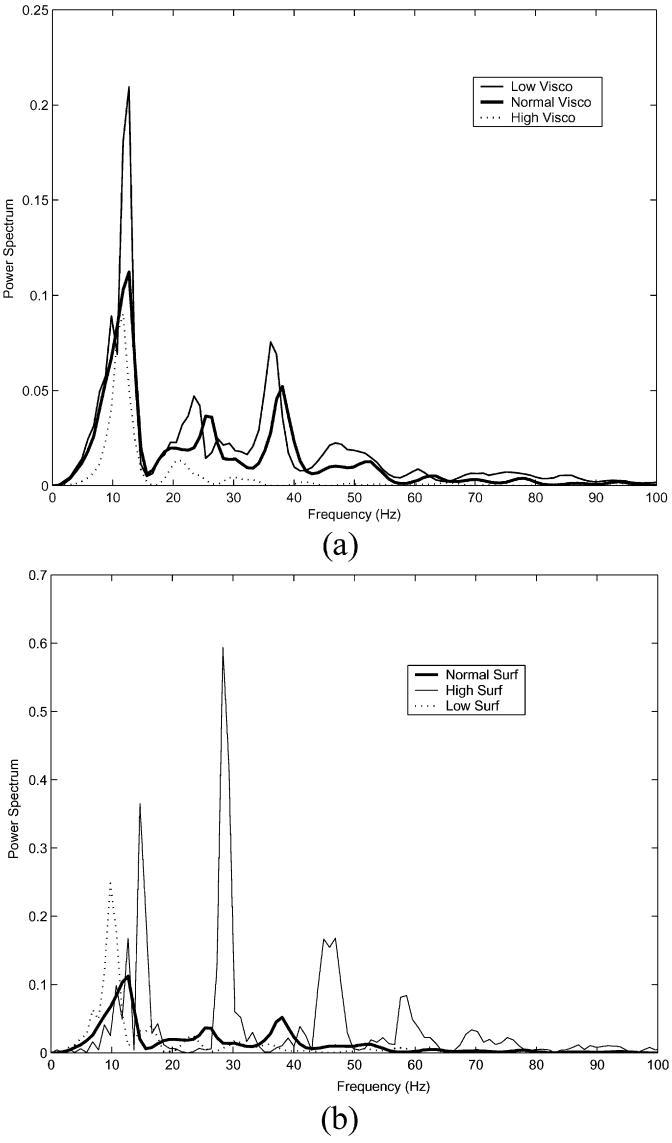

Fig. 7. Spectra of bubble bottom velocity oscillations: (a) viscosity effect; (b) surface tension effect.

nose takes on a slightly prolate spheroid shape due to the effect of the tube wall. Meanwhile, the bubble nose shape does not vary much between the different cases, although the bottom shape changes significantly. Moreover, velocity oscillations occur only at the bottom of the bubble, while velocity at the nose maintains a nearly constant value during bubble rise (Figs. 6(a)–(d)). It appears that the behavior of the bubble nose is independent of the parameters studied. However, a close examination of Fig. 6(c) reveals that the nose velocity curve is slightly wavy, which suggests that nose oscillations might occur if surface tension is sufficiently large. This needs further investigation in the future work.

4. Conclusions

The dynamics of a single gas bubble rising in a narrow vertical tube have been studied via a numerical method. The velocity field as well as the pressure distribution have been

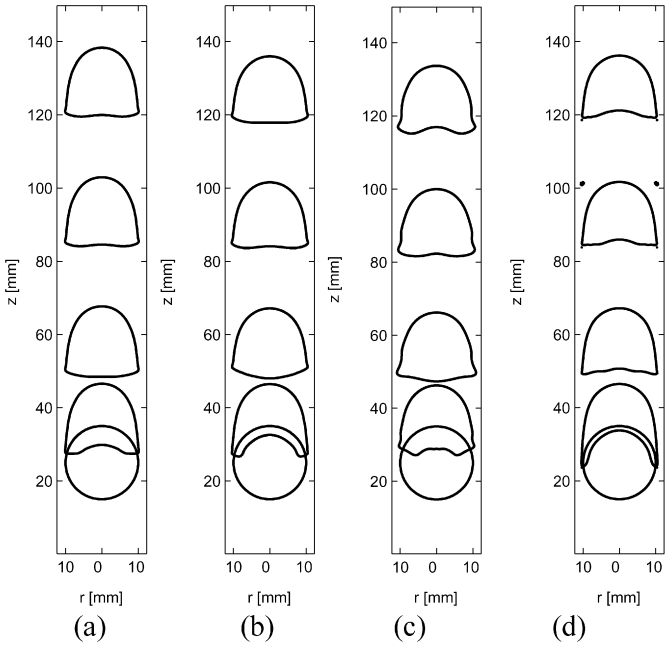

Fig. 8. Time evolution of the bubble shapes for different cases: (a) high viscosity; (b) low viscosity; (c) high surface tension; (d) low surface tension.

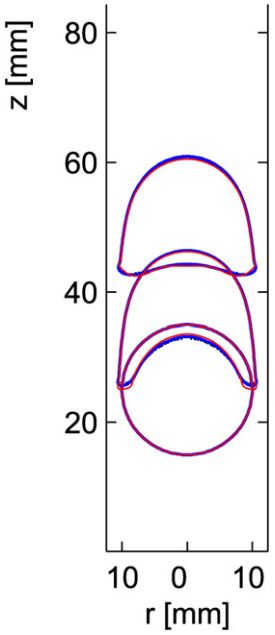

Fig. 9. Bubble deformations with different grid sizes (magnified view). Dot line: 0.5×0.5; solid line: 0.39×0.39; dash line: 0.25×0.25.

investigated and analyzed; the results obtained in the present study are in close agreement with experimental results reported in the literature. Special attention is paid to bubble oscillations at $Mo < 2.56 \times 10^{-7}$ and $Eo > 42.0$. It has been found that the bubble nose retains a relative stable shape while significant oscillations occur at the bubble bottom as it rises through the liquid from the static state. The parametric study shows that the liquid viscosity plays an important role in damping the oscillations without altering the oscillation frequency; while the surface tension significantly affects both the oscillation frequency and the amplitudes.

Appendix A. Grid refinement study

Computations have been conducted with three different mesh sizes for the grid sensitivity test. The magnified view of the bubble shapes at the initial stage with severe deformations is shown in Fig. 9. The results obtained from the three different grids are very close, which indicates the grid convergence is achieved.

References

[1] R. Clift, J.R. Grace, M.E. Webber, Bubbles, Drops, and Particles, Academic Press, New York, 1978.
[2] J. Fabre, A. Line, Modeling of two-phase slug flow, Annu. Rev. Fluid Mech. 24 (1992) 21–46.
[3] F. Viana, R. Pardo, R. Yanez, J.L. Trallero, D.D. Joseph, Universal correlation for the rise velocity of long gas bubbles in round pipes, J. Fluid Mech. 494 (2003) 379–398.
[4] R. van Hout, A. Gulitski, D. Barnea, L. Shemer, Experimental investigation of the velocity field induced by a Taylor bubble rising in stagnant water, Int. J. Multiphase Flow 28 (2002) 579–596.
[5] S. Polonsky, L. Shemer, D. Barnea, The relation between the Taylor bubble motion and the velocity field ahead of it, Int. J. Multiphase Flow 25 (1999) 957–975.
[6] J.D. Bugg, G.A. Saad, The velocity field around a Taylor bubble rising in a stagnant viscous fluid: numerical and experimental results, Int. J. Multiphase Flow 28 (2002) 791–803.
[7] J.D. Bugg, K. Mack, K.S. Rezkallah, A numerical model of Taylor bubbles rising through stagnant liquids in vertical tubes, Int. J. Multiphase Flow 24 (1998) 271–281.
[8] S. Polonsky, D. Barnea, L. Shemer, Averaged and time-dependent characteristics of the motion of an elongated bubble in a vertical pipe, Int. J. Multiphase Flow 25 (1999) 795–812.
[9] E. Kelley, M.M. Wu, Path instabilities of rising air bubble in a Hele–Shaw cell, Phys. Rev. Lett. 79 (7) (1997) 1265–1268.
[10] G. Mougin, J. Magnaudet, Path instability of a rising bubble, Phys. Rev. Lett. 88 (1) (2002) 014502.
[11] A.W.G. de Vries, A. Biesheuvel, L. van Wijngaarden, Notes on the path and wake of a gas bubble rising in pure water, Int. J. Multiphase Flow 28 (2002) 1823–1835.
[12] A.W.G. de Vries, Path and wake of a rising bubble, Ph.D. thesis, University of Twente, The Netherlands, 2001.
[13] A.Y. Tong, Z.Y. Wang, A numerical method for capillarity-dominant free surface flows, J. Comput. Phys. 221 (2007) 506–523.
[14] R. Scardovelli, S. Zaleski, Direct numerical simulation of free-surface and interfacial flow, Annu. Rev. Fluid Mech. 31 (1999) 567–603.
[15] G. Son, N. Hur, A coupled level set and volume-of-fluid method for the buoyancy-driven motion of fluid particles, Numer. Heat Transfer, Part B 42 (2002) 523–542.
[16] M. Sussman, E.G. Puckett, A coupled level set and volume-of-fluid method for computing 3D axisymmetric incompressible two-phase flows, J. Comput. Phys. 162 (2000) 301–337.
[17] Z.Y. Wang, Numerical study on capillarity-dominant free surface and interfacial flows, Ph.D. thesis, The University of Texas at Arlington, USA, 2006.
[18] H. Lamb, Hydrodynamics, Article 191, Cambridge University Press, Cambridge, 1932, pp. 284–290.